JOURNAL OF THERMOPHYSICS AND HEAT TRANSFER
Vol. 16, No. 4, October–December 2002

Heat Transfer Predictions in a Laminar Hypersonic Viscous/Inviscid Interaction

Datta V. Gaitonde* and Patrick W. Canupp†
U.S. Air Force Research Laboratory, Wright–Patterson Air Force Base, Ohio 45433
and
Michael S. Holden‡
Calspan—University at Buffalo Research Center, Buffalo, New York 14225

Results are documented of a blind validation study to characterize the accuracy of an upwind-biased finite volume method in predicting the surface loads caused by a laminar viscous/inviscid interaction. The effort supports a recent Research and Technology Organization code validation initiative and considers a benchmark configuration of the Working Group 10, consisting of Mach 9.5 flow past a 25/55 deg sharp-tipped double cone at a Reynolds number of 1.39435×10^6/m. Roe's flux-difference splitting scheme is employed with a nominally third-order reconstruction method and harmonic limiting. An extensive iterative- and grid-convergence study is performed to ensure solution accuracy. Comparison with experimental data shows that overall the numerical method reproduces the features of the interaction, including location and extent of separation to a degree that may be characterized as adequate for engineering purposes. However, upstream of separation and in the narrow peak heating region, discrepancies in heat transfer rates between computation and experiment range between 10 and 15% of maximum values. An exploration of the sensitivity of the solution to small variations (up to 10%) in several flow and numerical parameters reveals only modest influence on the nondimensionalized quantities.

Nomenclature

$C_{\mu 1}, C_{\mu 2}$	=	coefficients in Sutherland's law
c	=	speed of sound
c_v	=	specific heat at constant volume
E	=	total energy density
$\boldsymbol{F}$	=	z-direction flux vector
$\boldsymbol{G}$	=	r-direction flux vector
IL	=	number of points in z direction
J	=	cell Jacobian
$\hat{M}$	=	molecular weight of nitrogen
Pr	=	Prandtl number
p	=	pressure
Q	=	surface heat transfer rate
$\boldsymbol{Q}$	=	diagonalization matrix
q	=	heat flux
$\hat{R}$	=	universal gas constant
r	=	radial distance
$\bar{r}$	=	radial distance to centroid
$\boldsymbol{S}$	=	area vector of cell face
T	=	temperature
t	=	time
$\boldsymbol{U}$	=	vector of conserved variables
u	=	velocity component
$\boldsymbol{v}$	=	velocity vector
W	=	vector of primitive variables
$\boldsymbol{W}$	=	source term vector
z	=	axial distance
γ	=	ratio of specific heats
Δ	=	change
δ	=	small number for entropy cutoff
η	=	computational coordinate
κ	=	thermal conductivity; coefficient in reconstruction
Λ	=	eigenvalue matrix
μ	=	molecular viscosity
ν	=	area of cell
ξ	=	computational coordinate
ρ	=	density
τ	=	shear stress tensor
ϕ	=	coefficient in MUSCL method

Subscripts

r	=	radial
rms	=	root mean square
z	=	axial
θ	=	azimuthal

Superscripts

L	=	state on left side of interface
R	=	state on right side of interface
$\hat{}$	=	Roe-averaged state
$\tilde{}$	=	limited value

Received 15 October 2001; revision received 15 March 2002; accepted for publication 24 March 2002.

*Team Leader, High-Speed Flows, Computational Sciences Branch, VAAC. Associate Fellow AIAA.
†Visiting Research Scientist, VAAC. Member AIAA.
‡Program Manager, Aerooptics Evaluation Center. Associate Fellow AIAA.

I. Introduction

INTERACTIONS of shock waves with boundary layers, both laminar and turbulent, are of great significance in a variety of practical applications and have consequently been explored experimentally and numerically for several decades. In recent years, joint studies have yielded considerable insight into the physics of these phenomena. These efforts have also facilitated a critical evaluation of simulation accuracy. For example, in the three-dimensional interaction of crossing shocks with a turbulent boundary layer, comparison of numerical results with a variety of experimental data suggests that elements of the flow that are inviscid rotational are computed to reasonable accuracy.[1–4] These features include separation location, surface oil flow, surface pressure, and shock structure (for example, Ref. 5). It has been further noted these are controlled by the vorticity

in the incoming boundary layer and the strength and orientation of the shock wave.[6] These two items are computed accurately, the first because the turbulence model is effectively tuned for this purpose and the second because of the known accuracy of shock-capturing techniques. However, a major problem of numerical techniques is their tendency to overpredict grossly (by 100% or more[4,7]) heat transfer rates, which are of crucial significance in high-speed flows. This deficiency has been ascribed to inaccuracies in the turbulence modeling.[4] Indeed, as noted in Ref. 3, the flowfield near the surfaces is new in that it develops after attachment under complex three-dimensional pressure gradients, both favorable and adverse. Typical turbulence models fail to predict this situation accurately because they are generally developed for two-dimensional situations (for example, the discussion in Ref. 8).

Although there has been a degree of success in computing heat transfer rates and skin-friction coefficients in some laminar situations,[9,10] Candler et al.[11] have recently highlighted a hypersonic laminar viscous/inviscid interaction in which the discrepancies between computations and experiments are significant. To resolve this difficulty, carefully calibrated experiments have been conducted by Holden[12] and Holden and Wadhams[13] at Calspan—University of Buffalo Research Center to provide high-fidelity benchmark cases for computational efforts. Results from these experiments have been made available to support the efforts of Working Group (WG) 10 of the Research and Technology Organization (RTO). The present work responds to the call made by this organization to participate in a study to examine the capability of modern computational fluid dynamics methods by examining one of the benchmark cases, run 28, adopted by the RTO WG 10.[12] Some previous responses to this call may be found in Refs. 14–19.

We consider specifically the double-cone configuration (Fig. 1), which consists of two different cone half-angles with an upstream 25-deg section followed by a downstream 55-deg section. The model terminates with a right circular cylinder. Although experimental data have been obtained by Holden and Wadham[13] for both blunt and sharp nose tips, the present effort focuses only on the latter geometry.

The flow parameters consist of a nominal Mach number of 9.5 in a nitrogen medium and nominal Reynolds number per meter of 1.39435×10^6. Although data at higher Reynolds numbers have been reported, those cases will be considered in a later study. Under these conditions, complex shock–shock and shock–boundary-layer interactions dominate the flowfield. The flow is not only a challenging test case for hypersonic simulation techniques, but also helps illustrate the complex interactions that will occur around hypersonic flight vehicles. In addition to supporting the RTO code validation effort, the laminar and steady nature of the experimental data facilitates careful evaluation of the numerical model employed in earlier double-fin studies without the uncertainties associated with the turbulence model.

The numerical technique comprises several elements, including the method of solution reconstruction and limiting as well as the evaluation of fluxes from known cell-averaged states. We focus specifically on the Roe flux-difference split scheme with higher-order accuracy obtained through the MUSCL approach of van Leer.[20] This popular approach is incorporated into many production codes.

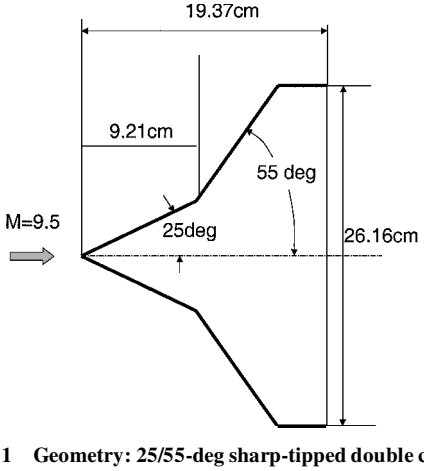

Fig. 1 Geometry: 25/55-deg sharp-tipped double cone.

Evaluation of the scheme is performed by comparison of the numerical results with experimental data for surface pressure as well as heat transfer rates. The governing equations are first outlined in Sec. II. For reference purposes, the complete description of the implementation, including the finite volume formulation, the flux-difference split scheme, the MUSCL approach, the entropy cutoff formulas, and the manner of simulating axisymmetry are presented in Sec. III. Section IV addresses the numerical issues associated with boundary condition implementation, time, and grid convergence and characterizes computational accuracy by comparison with experimental data. An extensive analysis of solution sensitivity to various parameters, both physical and numerical, is also performed.

II. Governing Equations

It is assumed that continuum conditions prevail: The results of Ref. 11 suggest that this is a reasonable approximation with the possible exception of the region in the immediate vicinity of the leading edge. Furthermore, the same source indicates that vibrational nonequilibrium as well as chemical reactions are of relatively little importance.

Because the flow is axisymmetric and noncontinuum effects are being ignored, the equations governing the development of the flow may be written as

$$\frac{\partial \boldsymbol{U}}{\partial t} + \frac{\partial \boldsymbol{F}}{\partial z} + \frac{1}{r}\frac{\partial r\boldsymbol{G}}{\partial r} = \frac{1}{r}\boldsymbol{W} \tag{1}$$

The vector of conserved quantities $\boldsymbol{U}$ and source term vector $\boldsymbol{W}$ are

$$\boldsymbol{U} = \begin{bmatrix} \rho \\ \rho u_z \\ \rho u_r \\ E \end{bmatrix} \qquad \boldsymbol{W} = \begin{bmatrix} 0 \\ 0 \\ p + \tau_{\theta\theta} \\ 0 \end{bmatrix} \tag{2}$$

where u_r and u_z are the velocities in the r and z directions and E is the total energy density of the gas. In terms of temperature T and specific heat at constant volume c_v,

$$E = \rho c_v T + \tfrac{1}{2}\rho\left(u_r^2 + u_z^2\right) \tag{3}$$

The flux vectors $\boldsymbol{F}$ and $\boldsymbol{G}$ are

$$\boldsymbol{F} = \begin{bmatrix} \rho u_z \\ \rho u_z^2 + p + \tau_{zz} \\ \rho u_z u_r + \tau_{zr} \\ (E + p)u_z + \tau_{zz}u_z + \tau_{zr}u_r + q_z \end{bmatrix} \tag{4}$$

$$\boldsymbol{G} = \begin{bmatrix} \rho u_r \\ \rho u_z u_r + \tau_{zr} \\ \rho u_r^2 + p + \tau_{rr} \\ (E + p)u_r + \tau_{zr}u_z + \tau_{rr}u_r + q_r \end{bmatrix} \tag{5}$$

The equation of state is

$$p = \rho(\hat{R}/\hat{M})T \tag{6}$$

Constitutive relations specify the stress tensor and heat flux vector in terms of flow gradients. The components of the viscous stress tensor are

$$\tau_{zz} = -\mu\left(2\frac{\partial u_z}{\partial z} - \frac{2}{3}\nabla \cdot \boldsymbol{v}\right) \tag{7}$$

$$\tau_{rr} = -\mu\left(2\frac{\partial u_r}{\partial r} - \frac{2}{3}\nabla \cdot \boldsymbol{v}\right) \tag{8}$$

$$\tau_{\theta\theta} = -\mu\left(2\frac{u_r}{r} - \frac{2}{3}\nabla\cdot\boldsymbol{v}\right) \tag{9}$$

$$\tau_{zr} = -\mu\left(\frac{\partial u_z}{\partial r} + \frac{\partial u_r}{\partial z}\right) \tag{10}$$

$$\nabla\cdot\boldsymbol{v} = \frac{\partial u_z}{\partial z} + \frac{1}{r}\frac{\partial(ru_r)}{\partial r} \tag{11}$$

and Fourier's law describes the heat flux vector

$$q_z = -\kappa\frac{\partial T}{\partial z}, \qquad q_r = -\kappa\frac{\partial T}{\partial r} \tag{12}$$

Sutherland's law gives the viscosity coefficient

$$\mu = C_{\mu 1}\left[T^{\frac{3}{2}}\Big/(T + C_{\mu 2})\right] \tag{13}$$

and the coefficient of thermal conductivity is

$$\kappa = \mu(c_v + \hat{R}/\hat{M})(1/Pr) \tag{14}$$

Unless otherwise mentioned, all calculations assume a nitrogen medium for which $C_v = 742$ J/kg·K, $C_{\mu 1} = 1.4\times 10^{-6}$ N·s/m^2, $C_{\mu 2} = 107$ K, $\gamma = 1.4$, and $Pr = 0.7$ (Ref. 21).

III. Numerical Method

The finite volume approach integrates governing equations over each cell in the discretized domain. For an axisymmetric flow, the cell is wedge shaped, and spatial integration spanning a three-dimensional volume gives

$$\int_{r_1}^{r_2}\int_{z_1}^{z_2}\int_{\theta}^{\theta+\Delta\theta}\frac{\partial \boldsymbol{U}_{i,j}}{\partial t} r\,\mathrm{d}\theta\,\mathrm{d}z\,\mathrm{d}r + \int_{r_1}^{r_2}\int_{z_1}^{z_2}\int_{\theta}^{\theta+\Delta\theta}\left(\frac{\partial \boldsymbol{F}}{\partial z}r + \frac{\partial(r\boldsymbol{G})}{\partial r}\right)\mathrm{d}\theta\,\mathrm{d}z\,\mathrm{d}r = \int_{r_1}^{r_2}\int_{z_1}^{z_2}\int_{\theta}^{\theta+\Delta\theta}\boldsymbol{W}_{i,j}\,\mathrm{d}\theta\,\mathrm{d}z\,\mathrm{d}r \tag{15}$$

Because in a given meridian plane ($\theta = \text{const}$)

$$\int_{r_1}^{r_2}\int_{z_1}^{z_2} r\,\mathrm{d}z\,\mathrm{d}r = \bar{r}\nu_{i,j} \tag{16}$$

where $\bar{r}$ and $\nu_{i,j}$ are the centroid and the area, respectively. Equation (16) further simplifies to

$$\bar{r}\nu_{i,j}\frac{\partial \boldsymbol{U}_{i,j}}{\partial t} + \int_S (r\boldsymbol{F}\boldsymbol{i} + r\boldsymbol{G}\boldsymbol{j})\cdot\mathrm{d}\boldsymbol{S} = \bar{r}\nu_{i,j}\boldsymbol{W}_{i,j} \tag{17}$$

or, in discrete form,

$$\bar{r}\nu_{i,j}\frac{\delta \boldsymbol{U}^n_{i,j}}{\Delta t} + \sum_{\text{sides}}(r\boldsymbol{F}^{n+1}\boldsymbol{i} + r\boldsymbol{G}^{n+1}\boldsymbol{j})\cdot\boldsymbol{S} = \bar{r}\nu_{i,j}\boldsymbol{W}^{n+1}_{i,j} \tag{18}$$

In this discretization, the average r coordinate of the cell approximates $\bar{r}$, whereas the average values of r on a particular cell face approximate the r values that appear inside the flux summation. Therefore, methods used for solving the two-dimensional form of the governing equations readily extend to axisymmetric flow with the addition of the source terms, multiplication of cell areas by $\bar{r}$, and scaling of cell face metrics by r.

Time integration is achieved with an implicit residual driven line Gauss–Seidel relaxation scheme as described in Ref. 22. With first-order Euler implicit time discretization and linearization of the fluxes in time, the discretized equation may be written in the form

$$\{\text{NUMERICS}\}\,\delta\boldsymbol{U} = \text{PHYSICS} \tag{19}$$

where PHYSICS represents the residual, NUMERICS contains the driving terms, and $\delta\boldsymbol{U}$ denotes the change in the solution vector at each time step. The full Navier–Stokes equations are utilized in computing the residual with the upwind-biased method for the inviscid terms and centered evaluation of the viscous terms. One advantage of the methodology is that approximations may be utilized in the NUMERICS portion of the code without affecting the accuracy of the converged result. In fact, Liou and van Leer[23] point out that the use of Steger–Warming splitting in evaluating the NUMERICS portion leads to robust codes for the Newton linearization procedure even if the PHYSICS term is evaluated with other methods (such as van Leer's splitting[20] or Roe's upwinding[24]). The implicit operator in the present effort, therefore, utilizes the Steger–Warming Jacobians to obtain strong diagonal dominance. For simplicity the viscous Jacobians in the driving NUMERICS portion are computed with the thin-layer approximation.

When solved with the Gauss–Seidel line relaxation procedure, Eq. (19) represents a block tridiagonal system. The method is unconditionally stable for model diffusion and convection equations and is also known to be relatively insensitive to the choice of time increment per iteration.[25]

At each cell face, the state of the flow is described by two vectors of conserved variables, $\boldsymbol{U}^L$ and $\boldsymbol{U}^R$ on either side of the interface. These vectors are obtained by extrapolation from the known values of cell-averages with the MUSCL approach in conjunction with a limiter as described next.

Roe's flux-difference-split formula may be written as[24]

$$\boldsymbol{G}_{j+\frac{1}{2}} = \tfrac{1}{2}[\boldsymbol{G}(\boldsymbol{U}^L) + \boldsymbol{G}(\boldsymbol{U}^R)] - \tfrac{1}{2}\hat{Q}|\hat{\Lambda}|\hat{Q}^{-1}(\boldsymbol{U}^R - \boldsymbol{U}^L) \tag{20}$$

where the caret indicates evaluation at the Roe-averaged state between $\boldsymbol{U}^L$ and $\boldsymbol{U}^R$ (Ref. 24). A similar expression holds for the vector $\boldsymbol{F}$. To enforce the entropy conditon, following Harten,[26] the eigenvalues λ of A are modified when they are below some small threshold δ:

$$|\lambda| = |\lambda^2 + \delta^2|/2\delta, \qquad |\lambda| < \delta \tag{21}$$

In the body-normal direction, an isotropic form is utilized for δ (Ref. 27):

$$\delta = \tilde{\delta}J^{-1}[|\boldsymbol{u}\cdot\nabla\xi| + |\boldsymbol{u}\cdot\nabla\eta| + (c/2)(|\nabla\xi| + |\nabla\eta|)] \tag{22}$$

where $\tilde{\delta}$ is a specified constant. To prevent excessive dissipation in the streamwise direction due to the cell aspect ratio, an anisotropic cutoff formula described by Müller[28] is employed in that direction:

$$\delta = \tilde{\delta}J^{-1}\lambda^{(\xi)}\left\{1 + \left[\lambda^{(\eta)}\Big/\lambda^{(\xi)}\right]^{\frac{2}{3}}\right\} \tag{23}$$

where $\lambda^{(k)} = |\boldsymbol{u}\cdot\nabla k| + c|\nabla k|$. The value of $\tilde{\delta}$ utilized is 0.01.

The order of accuracy of the finite volume scheme is dictated by the reconstruction of the states $\boldsymbol{U}^L$ and $\boldsymbol{U}^R$ from the known values of the average of the solution vector in adjacent cells. The present method adopts the upwind-biased MUSCL algorithm due to van Leer[29] and Anderson et al.[30] The conserved vectors $\boldsymbol{U}^L$ and $\boldsymbol{U}^R$ are obtained by reconstructing the solution in terms of the primitive variables $W = \{\rho, u, v, p\}$ by a windward-biased formula:

$$W^L_{j+\frac{1}{2}} = W_j + (\phi/4)[(1-\kappa)\tilde{\nabla} + (1+\kappa)\tilde{\Delta}]W_j \tag{24}$$

$$W^R_{j+\frac{1}{2}} = W_{j+1} - (\phi/4)[(1+\kappa)\tilde{\nabla} + (1-\kappa)\tilde{\Delta}]W_{j+1} \tag{25}$$

Two popular methods based on the described stencil are the third-order (for linear systems) method, where $\phi = 1$ and $\kappa = \frac{1}{3}$, and the second-order fully upwind method, where $\phi = 1$ and $\kappa = -1$. In the presence of shocks, higher-order methods yield spurious oscillations, which must be eliminated by use of a monotonicity-preserving limiter. The limiter function is introduced by defining Δ as

$$\tilde{\Delta}_{j+\frac{1}{2}} = f\left(\Delta_{j+\frac{1}{2}}, \Delta_{j-\frac{1}{2}}\right), \qquad \Delta_{j+\frac{1}{2}} = W_{j+1} - W_{j-1} \tag{26}$$

A similar equation applies to $\tilde{\nabla}$. The limiter is a crucial component of the overall algorithm, exerting significant influence on the accuracy of the calculation. Here, we primarily employ the harmonic limiter[20]

$$f(x, y) = \frac{x \cdot y + |x \cdot y|}{|x| + |y| + \epsilon} \tag{27}$$

where ϵ is a small number to prevent division by zero.

Second-order central schemes are employed to approximate the derivatives that appear in the viscous fluxes. These are computed in a straightforward manner and are not detailed here.

IV. Results

A. Boundary Conditions and Computational Grids

The boundary conditions are couched in finite volume formulation as summarized in Fig. 2. At the axis of symmetry, upstream of the body, the total flux $\boldsymbol{F}$, including both inviscid and viscous components, is zero because the projected area of the cell face is zero. At all points on the far-field boundary, the freestream flow vector is specified according to the known published conditions established in the experiments. Thus, the Mach number is $M = 9.59$, the Reynolds number is $Re = 1.39435 \times 10^6$/m, the freestream temperature is $T_\infty = 185.6$ K, and the wall temperature is $T_w = 293.3$ K. At the downstream boundary, the zero gradient condition is employed. It is essential, therefore, that the outer boundary be placed far enough away that the shock envelope exits the domain at the downstream boundary and that the flow at this boundary be predominantly supersonic. At the body surface, a pseudocell approach is employed to specify no-slip, zero pressure gradient, and a constant surface temperature. The inviscid flux is specified based on the pressure and surface normals, whereas the viscous flux is computed in the usual fashion.

The general form of the grid is shown in Fig. 3, where every fourth point in each direction is plotted on the coarsest grid employed. Solutions are obtained on four grids of increasing mesh density as listed in Table 1, all obtained courtesy of Candler et al.[11] with the only difference that a few points were added at the outer edge to prevent shock interaction with the outer boundary during transients. Although the mesh is not orthogonal at the surface, and this has some implication on the implementation of the zero wall-normal pressure gradient, grid resolution studies suggest that the effects of this imperfection are negligible.

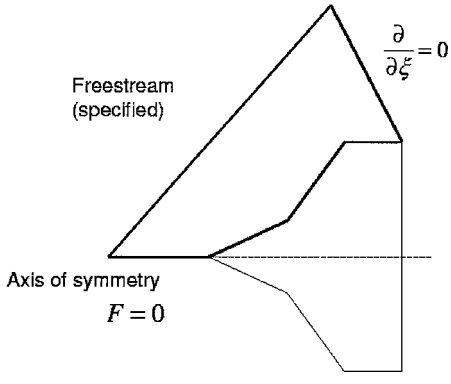

Axis, freestream and downstream

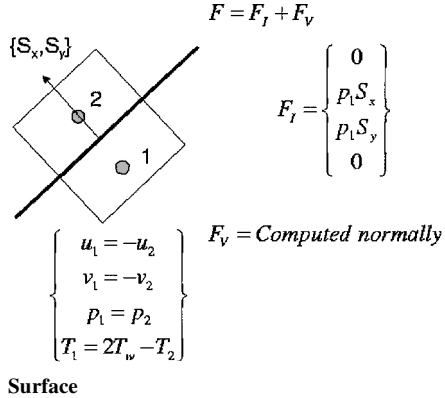

Surface

Fig. 2 Implementation of boundary conditions.

Table 1 Sizes of meshes employed

Grid	Size ($IL \times JL$)[a]
1	256×138
2	512×266
3	1024×522
4	1024×1034

[a] IL points in streamwise direction and JL points in radial direction

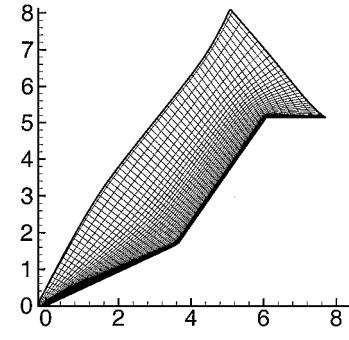

Fig. 3 Structure of grid employed; every fourth line plotted on coarsest mesh.

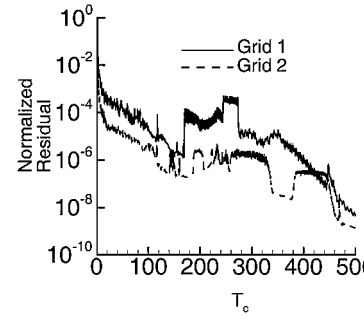

Grids 1 and 2

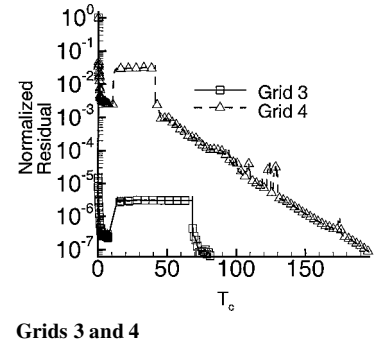

Grids 3 and 4

Fig. 4 Global residual history.

B. Time Convergence History

Convergence is determined for all computations by monitoring several quantities. The primary quantity is the global residual (GR) defined as

$$\|\mathrm{GR}\| = \frac{1}{(IL)(JL)} \sqrt{\sum_{i=1}^{IL} \sum_{j=1}^{JL} \sum_{k=1}^{4} \left(\frac{(R_k)_{i,j}}{\boldsymbol{U}_{\infty,k}} \right)^2} \tag{28}$$

where k denotes the kth component, $(R_k)_{i,j}$ is the change in the flow solution, $R_k = \Delta \boldsymbol{U}_k$ at i, j, and $\boldsymbol{U}_\infty = \{\rho, \rho u_z, \rho u_z, E\}_\infty$. The variation of the GR for each mesh is shown in Fig. 4. Grids 3 and

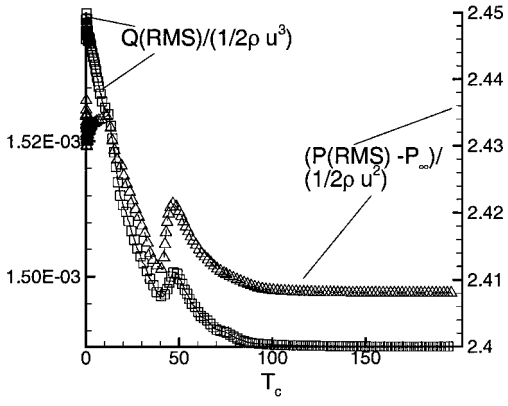

a) Integrated surface rms pressure and heat transfer

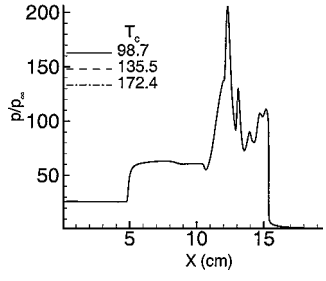

b) Surface pressure

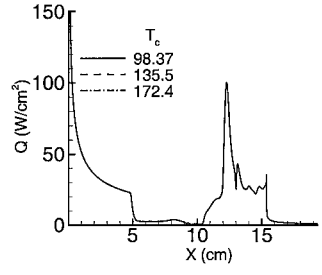

c) Heat transfer rate

Fig. 5 Time convergence of surface quantities.

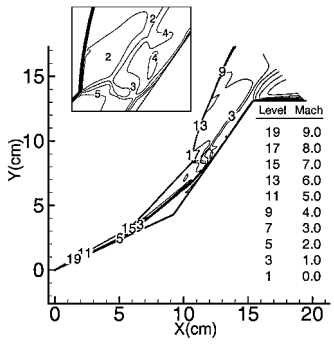

Mach number

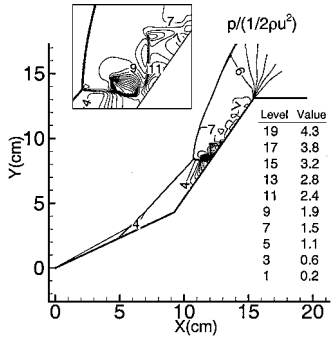

Pressure

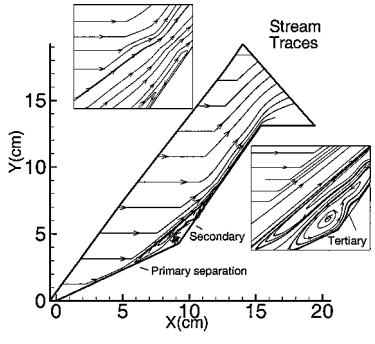

Stream traces

Fig. 6 Overall features of computed flow.

4 require less time to achieve the reduction in residual primarily because the converged result on grid 1 was interpolated to obtain a better initial condition on these meshes. For plotting purposes, results have been normalized by the value of $\|GR\|$ obtained after the first iteration. Irregular patterns in the residual represent variations in the time-step sizes that were employed in attempts to increase convergence rate. The solutions on all grids show residual declines of at least seven orders of magnitude.

In addition to the residual, the integrated root mean square pressure and heat transfer values over the entire surface are also monitored. Results for grid 4 are plotted in Fig. 5a. With P and Q denoting pressure and heat transfer, respectively,

$$(P)_{\text{rms}} = \frac{1}{IL}\sqrt{\sum_{i=1}^{IL}\left(\frac{p_{i,j=\text{surface}}}{p_\infty}\right)^2} \tag{29}$$

$$(Q)_{\text{rms}} = \frac{1}{IL}\sqrt{\sum_{i=1}^{IL}(Q_{i,j=\text{surface}})^2} \tag{30}$$

Figure 5a shows that the values of these two quantities achieve a constant value beyond about $100T_c$, where T_c is the characteristic time, that is, the time required to traverse the domain at freestream velocity. (Note, however, that because a nonlinear update is employed in the Gauss–Seidel relaxation process, the calculations are not strictly time accurate.) Figures 5b and 5c show surface pressure and heat transfer rates at several instants during the time evolution. The solution is observed to be converged along the entire surface, including in the region of relatively sharp peak values and in the rapid spatial variations downstream.

C. Overall Features of Computed Flow

To set the context for the subsequent discussion, the overall structure of the flowfield is shown in Fig. 6 in terms of the Mach number, pressure, and stream traces. The features of the flowfield have been elucidated in some detail by Wright et al.,[31] who considered flow past a 25/50 deg double cone at Mach 8 and at Reynolds numbers 2.7×10^5, and 4.8×10^5, which are higher than those considered here. However, the overall structure is similar to the present lower Reynolds number results and may be described in the framework of the type V interaction of Edney.[32] Considered independently, both cone angles yield weak shocks at the freestream Mach number considered. The connecting shock forms two triple points: the first with the forecone and separation shocks and the second with the aft cone and reattachment shocks. A shear layer emanates from the aft triple point effectively separating the subsonic flow from the near-wall supersonic jet. The viscous interaction associated with the reattachment shock is similar to that described for transonic interactions (for example, Ref. 33). Analysis of the stream traces shows separation of the nose-cone boundary layer well upstream of the corner, and reattachment before the formation of the supersonic vortex. The separated region itself comprises three counter-rotating cells, indicating the occurrence of both secondary and tertiary separation.

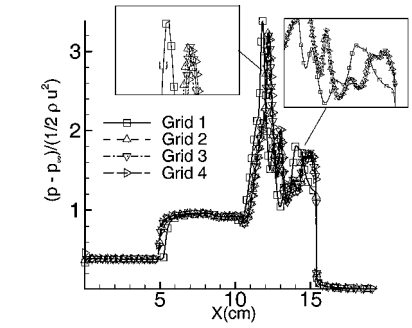

Surface pressure

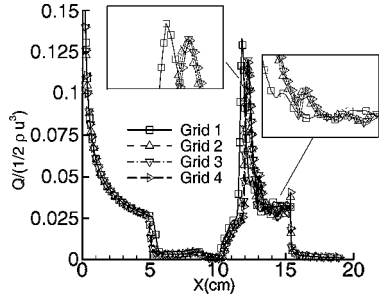

Heat transfer

Fig. 7 Grid convergence of surface quantities.

D. Grid Convergence

As noted earlier, solutions were obtained on four different meshes. Figure 7 indicates the level of grid convergence achieved in terms of the surface pressure and heat transfer rates. Compared to the other meshes, the coarsest grid exhibits delayed upstream influence and separation. Furthermore, the peak values of both heat transfer and pressure are located upstream of those on the finer meshes and are slightly larger. In contrast, results on grids 2–4 differ little from each other: Peak level variation between meshes 2 and 4 is under 3% for pressure and heat transfer, indicating that the flow is adequately resolved. Interestingly, results on all grids are in close agreement upstream of separation, despite the large gradients and heat transfer rates in this region. The viscous/inviscid interaction downstream clearly introduces finer scales of motion, requiring the greater resolution of the finer meshes.

To explore grid convergence away from the surface, the flowfield was probed at nine stations shown in Fig. 8a. The first three are located on the first cone, the fourth is at the corner, and the remaining five are on the second cone. Figure 8b exhibits Mach number profiles at several of these locations. Note that, for all stations, the lower value of the ordinate starts at the body surface and does not extend to the freestream for the last station plotted. All grids predict the same trends, with results on grids 2–4 being in close agreement with each other. Shocks outside of the viscous/inviscid interaction region are captured within one or two cells, depending on the local degree of grid alignment with the shock. The coarsest mesh, however, shows significant oscillations at station $X/L_{\text{cone}} = 1.125$. This is a drawback of the highly compressive limiter employed. The supersonic wall jet is most clearly evident at $X/L_{\text{cone}} = 1.375$, where the Mach number goes from supersonic near the wall but becomes subsonic beyond the shear layer.

E. Comparison with Experimental Data

Results on grid 4 were submitted to the WG 10 as part of a blind study and were subsequently compared with experimental data in Ref. 34. These results are replotted in Fig. 9 in terms of the pressure and heat transfer coefficients. The error associated with the experimental data has been discussed in Ref. 13 and may be specified as $\pm 3\%$ for surface pressure and $\pm 5\%$ for heat transfer measurements. Overall, the computational accuracy may be characterized as reasonable for most engineering purposes. The surface pressure on the

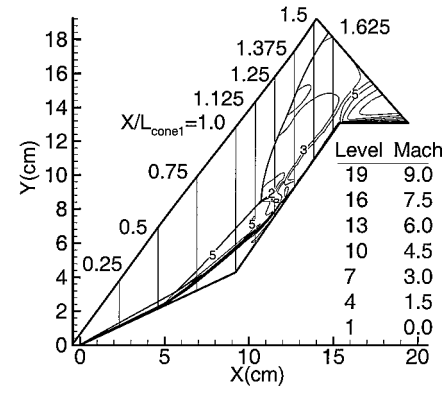

a) Stations

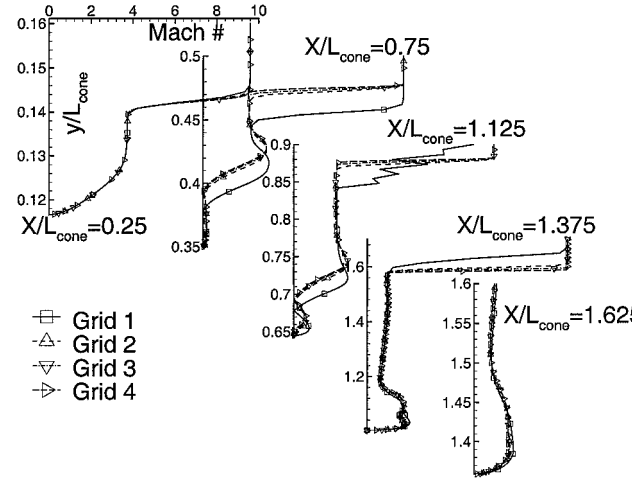

b) Mach number

Fig. 8 Grid convergence of quantities in flowfield.

first cone is roughly constant and agrees with the value derived from inviscid conical flow analysis downstream of the leading shock. A plateau between $5 < X < 10$ cm follows the rapid rise observed at the location of separation, $X \sim 5$ cm. A second sharp increase in pressure occurs in the vicinity of reattachment. The peak computed pressure coefficient is about 3.2, which corresponds to $p/p_\infty \sim 205$. The location of the computed peak is about 4% downstream of the experimental observation whereas the magnitude differs by about 3%. These numbers are qualified, of course, by that experimental measurements are made on a much coarser grid. Consequently, measured peaks may be smaller than actual values. Downstream of the peak, the surface pressure exhibits spatial oscillations. Whereas the experiments show a single local peak, the computations indicate a more intricate pattern. Further analysis indicates a correlation of these extrema with the impingement of components of the wave train between the wall and the shear layer and originating at the aft triple point.

Heat transfer data (Fig. 9b) show more differences between computation and experiment than pressure, but the former still yields a reasonable engineering approximation. The streamwise drop in heat transfer from the high values anticipated at the tip is more rapid in the experiment. The relative error in the upstream region is about 30% when normalized with local values, or roughly 10% relative to the peak. The magnitudes of the relatively low values of heat transfer downstream of separation are predicted accurately by the computation. Both computations and experiment show a sharp rise and fall in heat transfer rate near reattachment, the entire region being less than 2.5 cm in length. The rapid rise is delayed in the computation, leading to a peak heating rate that is downstream of the experimental observation by about 10% relative to the length of the first cone and that is overpredicted by about 15%, where, again, the earlier qualification regarding finitely spaced experimental observations holds. Downstream of the peak, the computed heat

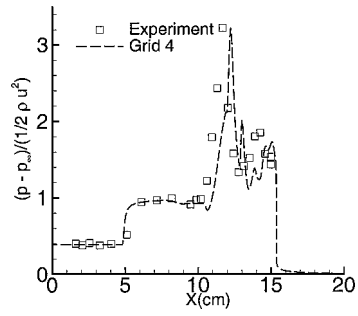

a) Surface pressure

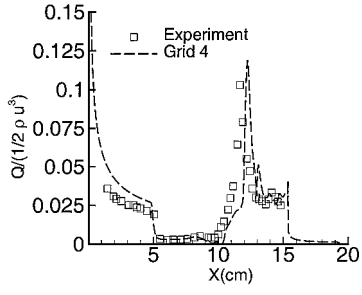

b) Heat transfer rate

Fig. 9 Comparison with experiment.

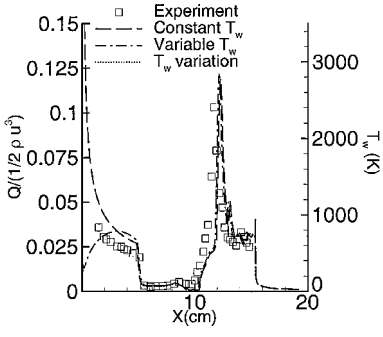

Fig. 10 Effect of adiabatic tip on heat transfer rate.

transfer rate shows the localized peak similar to that observed in the pressure. Experiments, however, show a more gradual single-cycle undulation.

A preliminary attempt has been made to explore issues related to the specification of the wall temperature in the computation. As noted earlier, the wall temperature was assumed constant along the entire model. A separate computation was run on grid 2 with a variable temperature profile determined as follows. Although unrealistic, it was assumed that the tip of the model achieves adiabatic conditions and that the wall temperature subsequently relaxes, smoothly obtaining the value T_w over a distance extending from the tip to a point chosen arbitrarily to be located slightly upstream of the point of separation ($X/L_{\text{cone}} = \Delta = 1.8$). In this range, the wall temperature is specified by a cubic polynomial:

$$T = x^3 + C_1 x^2 + C_2 x + C_3 \tag{31}$$

whose constants are determined by the three conditions: $T = T_{\text{aw}}$ at $x = 0$ and both $T = T_w$ and its streamwise derivative $\partial T/\partial x = 0$ at $x = \Delta$. Expressions for the coefficients in Eq. (31) may be found in Ref. 35. Note that T_{aw} is not specified explicitly but rather evolves in the computation from the condition that the flow is adiabatic at the tip. The surface temperature variation obtained at steady state, shown in Fig. 10, obtains its peak close to the expected adiabatic value at the leading edge and drops in the desired fashion. Although high-temperature phenomena are anticipated to mute these high values significantly, these effects were not taken into account in the present study. The conclusion of Ref. 11 that nonequilibrium effects are negligible may require reevaluation in the present case where wall conditions are modified. The impact of the hypothetical

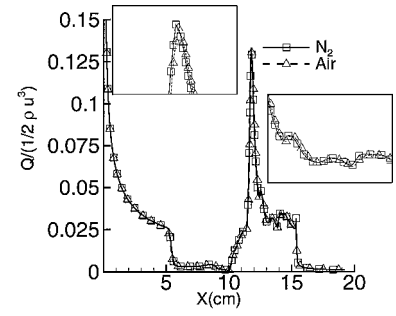

a) N_2 vs air

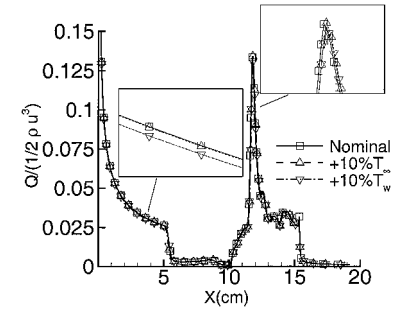

b) Freestream and wall temperature variation

Fig. 11 Effect of small perturbations in gas and flow parameters on heat transfer rate.

temperature profile on heat transfer is also shown in Fig. 10. Although the surface pressure is not affected in any significant fashion (not shown), as anticipated the heat transfer rate rises rapidly from its zero value at the tip and overshoots the experimental measurements. At some locations just before separation, the heat transfer rate exceeds that obtained with the constant wall-temperature condition. However, there is negligible impact at or downstream of separation. These results suggest that the consistent discrepancies upstream of separation have their root cause in some other as yet unknown mechanism.

F. Solution Sensitivity to Various Parameters

The sensitivity of the solution to specification of various parameters such as gas properties, Mach number, and Reynolds number was explored by examining the impact of modest perturbations in these quantities on surface pressure and heat transfer. To reduce the computational burden, unless otherwise specified these computations were performed on mesh 1.

Figure 11a exhibits the effect of variation of gas properties on heat transfer rates. As noted earlier, all calculations described were performed for N_2 for which gas properties were presented earlier. Figure 11 also shows results obtained with air as the medium, assuming $C_v = 717.55$ J/kg · K, $C_{\mu 1} = 1.45 \times 10^{-6}$ N · s/m^2, and $C_{\mu 2} = 110.4$ K. Although the physical values of the surface pressure and heat transfer differ in the two calculations, no significant deviation is observed when the standard normalization is employed. Figure 11b exhibits the effect of varying freestream and wall temperature (for N_2). In the first numerical experiment, the freestream temperature was raised by 10% of the nominal value, whereas in the second, T_∞ was reset to its original value and the wall temperature was raised by 10% over the entire surface. Despite the change in freestream total energy by 13.7%, the effect of freestream temperature on normalized heat transfer rate is seen to be negligible, whereas a detailed examination of the effect of raising the wall temperature shows that heat transfer changes by a very small amount (~1%).

Figures 12a and 12b show the effect of perturbing the Mach number and Reynolds number, respectively. In the first case, the Mach number was increased to 10.1 from the nominal value of 9.59. A reduction was not explored to avoid the situation where the shock due to the downstream 55-deg cone detaches. The upstream influence is seen to diminish at the higher Mach number, whereas the peak

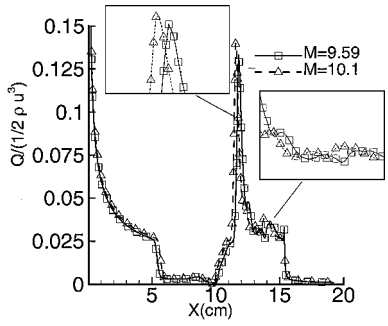

a) Mach number

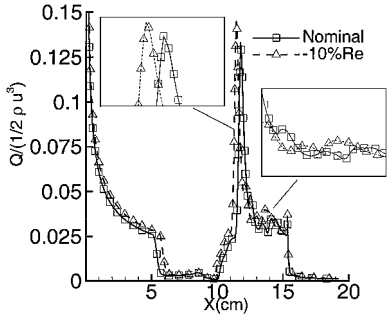

b) Reynolds number

Fig. 12 Effect of Mach and Reynolds number variation on surface heat transfer.

heat transfer value increases and its location moves upstream. These trends are consistent with those observed in other laminar shock–boundary-layer interactions (for example, Ref. 36): For example, the upstream influence is affected by the height of the subsonic region, which decreases with increasing Mach number.

Figure 12b shows the effect of a moderate 10% reduction in Reynolds number on the heat transfer rate. The sensitivity to Reynolds number is greater than to the Mach number, and in particular, the heat transfer rate before separation is higher and separation is delayed. These trends also mirror the observations in classical literature on other similar interactions (for example, Refs. 37 and 38). This may again be correlated to shock–laminar boundary-layer interaction theory in terms of the skin-friction coefficient. Because the skin-friction coefficient diminishes with distance downstream of the leading edge, the momentum thickness at a fixed distance from the leading edge is smaller for the lower-Reynolds-number case. In this sense, the boundary layer is more robust to adverse pressure gradients, and the trend is consistent with reduction in upstream influence of the corner. Although the impact of the Mach and Reynolds numbers is not insignificant, the preceding results suggest that the observed consistent discrepancy between experimental and computed heat transfer rates before separation are unrelated to parameter specification.

The limiter employed to enforce monotonicity is known to be critical to solution accuracy. In Ref. 10, for example, the impact of a limiter on heat transfer and skin-friction coefficient in blunt-body and compression corner flows has been shown to be significant, especially on coarser meshes. A similar sensitivity was observed in Ref. 16 to surface pressure and separation region. In the present work, to study the impact of a limiter, the harmonic formula [Eq. (27)] was replaced with the minmod limiter on grid 2; all other components of the algorithm remaining the same. The minmod limiter is expressed as

$$f(x, y) = \text{minmod}(x, y)$$

$$= \text{sgn}(x) \cdot \max\{0, \min[|x|, y\,\text{sgn}(x)]\} \tag{32}$$

The effect of this change is shown in Fig. 13 for heat transfer rates, where the trends observed are similar to those in surface pressure, together with results from grid 4. For the purposes of numerical

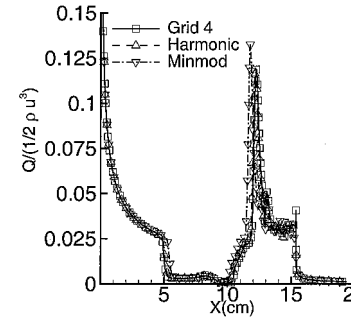

Fig. 13 Effect of limiter.

analysis, grid converged results rather than experimental data are the standard. In the interaction region, the predictions with the minmod limiter are not unlike those obtained when the Reynolds number was reduced (Fig. 12) with a delay in separation, a shortened separation region, and an increase in peak value. In this sense, the minmod limiter may be termed more diffusive, mirroring the trends observed in Refs. 10 and 16.

V. Conclusions

An extensive study has been performed to evaluate the accuracy of a popular high-resolution upwind-biased scheme based on Roe's flux-difference-split approach[24] by comparison with newly obtained data for a viscous/inviscid interaction at Mach 9.5. The flow past a 25/55 deg sharp-tipped double-cone configuration is computed at a Reynolds number of 1.39435×10^6/m, which is small enough to justify the greatly simplifying assumption of laminar flow. The freestream and wall temperatures are also low enough that previous studies indicating relatively insignificant high-temperature effects are pertinent. A detailed time and grid convergence study has been performed to demonstrate that the computations represent discrete solutions to the governing axisymmetric Navier–Stokes equations. Comparison with experimental data exhibits good agreement in overall trends, in size and location of the separation region, and in the surface pressure distribution. A consistent error of about 10% based on peak heating values is observed upstream of separation, and the maximum value is overpredicted by about 15%. These discrepancies are much smaller than those observed in turbulent shock–boundary-layer interactions, which provides additional confirmation that the source of error in those cases is the turbulence model employed. A study of solution sensitivity to several parameters indicates that modest changes in gas parameters (air vs nitrogen), wall temperature, and freestream temperature (10%) have no significant impact on normalized surface loading. Variations in Mach and Reynolds numbers have a perceptible influence on the solution, with trends predictable from the literature of shock–laminar boundary-layer interactions, but do not explain the noted discrepancies. Future effort will focus on examining higher-Reynolds-number cases.

Acknowledgments

This work was sponsored by the Air Force Office of Scientific Research under tasks monitored by William Hilbun, Steven Walker, and John Schmisseur. It was also supported in part by a grant of computer time from the Department of Defense High Performance Computing Shared Resource Centers at the Naval Oceanographic Office. The authors thank Graham Candler for providing the grids employed and acknowledge several useful conversations with Joseph Shang and Miguel Visbal. We also thank John Schmisseur for help in preparing this paper.

References

[1] Schmisseur, J., and Gaitonde, D., "Numerical Investigation of New Topologies in Strong Crossing Shock-Wave/Turbulent Boundary-Layer Interactions," AIAA Paper 2000-0931, Jan. 2000.

[2] Thivet, F., Knight, D., Zheltovodov, A., and Maksimov, A., "Some Insights in Turbulence Modeling for Crossing-Shock-Wave/Boundary-Layer Interactions," AIAA Paper 2000-0131, Jan. 2000.

[3]Gaitonde, D., and Shang, J., "Skin-Friction Predictions in a Crossing-Shock Turbulent Interaction," *Journal of Propulsion and Power*, Vol. 13, No. 3, 1997, pp. 342–348.

[4]Knight, D., and Degrez, G., "Shock Wave Boundary Layer Interactions in High Mach Number Flows—A Critical Survey of Current CFD Prediction Capabilities," TR AR-319, Vol. 2, AGARD, 1997.

[5]Gaitonde, D., Shang, J., Garrison, T., Zheltovodov, A., and Maksimov, A., "Three-Dimensional Turbulent Interactions Caused by Asymmetric Crossing-Shock Configurations," *AIAA Journal*, Vol. 37, No. 12, 1999, pp. 1602–1608.

[6]Gaitonde, D., Visbal, M., Shang, J., Zheltovodov, A., and Maksimov, A., "Parameteric Investigation of Flowfield Structure and Validation Issues in 3-D Crossing-Shock Wave/Turbulent Boundary Layer Interactions," *International Conference on Methods of Aerophysical Research (ICMAR)*, No. 9, 1998.

[7]Zha, G.-C., and Knight, D., "Three-Dimensional Shock/Boundary-Layer Interaction Using Reynolds Stress Equation Turbulence Model," *AIAA Journal*, Vol. 34, No. 7, 1996, pp. 1313–1318.

[8]Bradshaw, P., "Turbulence: The Chief Outstanding Difficulty of Our Subject," *Experiments in Fluids*, Vol. 16, No. 3/4, 1994, pp. 203–216.

[9]Prabhu, R., Stewart, J., and Thareja, R., "Shock Interference Studies on a Circular Cylinder at Mach 16," AIAA Paper 90-0606, Jan. 1990.

[10]Gaitonde, D., and Shang, J., "Accuracy of Flux-Split Algorithms in High-Speed Viscous Flows," *AIAA Journal*, Vol. 31, No. 7, 1993, pp. 1215–1221.

[11]Candler, G., Nompelis, I., and Holden, M., "Computational Analysis of Hypersonic Laminar Viscous–Inviscid Interactions," AIAA Paper 2000-0532, Jan. 2000.

[12]Holden, M., "Experimental Studies of Laminar Separated Flows Induced by Shock Wave/Boundary Layer and Shock/Shock Interaction in Hypersonic Flows for CFD Validation," AIAA Paper 2000-0930, Jan. 2000.

[13]Holden, M., and Wadhams, T., "Code Validation Study of Laminar Shock/Boundary Layer and Shock/Shock Interactions in Hypersonic Flow. Part A: Experimental Measurements," AIAA Paper 2001-1031, Jan. 2001.

[14]Kato, H., and Tannehill, J., "Computation of Hypersonic Laminar Separated Flows using an Iterated PNS Algorithm," AIAA Paper 2001-1028, Jan. 2001.

[15]Boyd, I., and Wang, W.-L., "Monte Carlo Computations of Hypersonic Interacting Flows," AIAA Paper 2001-1029, Jan. 2001.

[16]Candler, G., Nompelis, I., and Druguet, M.-C., Navier–Stokes Predictions of Hypersonic Double-Cone and Cylinder-Flare Flowfields," AIAA Paper 2001-1024, Jan. 2001.

[17]Moss, J., "DSMC Computations for Regions of Shock/Shock and Shock/Boundary Layer Interaction," AIAA Paper 2001-1027, Jan. 2001.

[18]Gnoffo, P., "CFD Validation Studies for Hypersonic Flow Prediction," AIAA Paper 2001-1025, Jan. 2001.

[19]Roy, C., Bartel, T., Gallis, M., and Payne, J., "DSMC and Navier–Stokes Predictions for Hypersonic Laminar Interacting Flows," AIAA Paper 2001-1030, Jan. 2001.

[20]van Leer, B., "Towards the Ultimate Conservation Difference Scheme V, A Second-Order Sequel to Godunov's Method," *Journal of Computational Physics*, Vol. 32, No. 1, 1979, pp. 101–136.

[21]White, F., *Viscous Fluid Flow*, McGraw–Hill, New York, 1991, pp. 27–32.

[22]MacCormack, R., "Current Status of Numerical Solutions of the Navier–Stokes Equations," AIAA Paper 85-0032, Jan. 1985.

[23]Liou, M.-S., and van Leer, B., "Choice of Implicit and Explicit Operators for the Upwind Differencing Method," AIAA Paper 88-0624, Jan. 1988.

[24]Roe, P., "Approximate Riemann Solvers, Parameter Vectors and Difference Schemes," *Journal of Computational Physics*, Vol. 43, No. 2, 1981, pp. 357–372.

[25]Thomas, J., and Walters, R., "Upwind Relaxation Algorithms for the Navier Stokes Equations," *AIAA Journal*, Vol. 25, No. 4, 1987, pp. 527–534; also AIAA Paper 85-1501, July 1985.

[26]Harten, A., "High Resolution Schemes for Hyperbolic Conservation Laws," *Journal of Computational Physics*, Vol. 49, No. 3, 1983, pp. 357–393.

[27]Yee, H., "Upwind and Symmetric Shock-Capturing Schemes," NASA, TM, TR 89464, 1987.

[28]Müller, B., "Simple Improvements of an Upwind TVD Scheme for Hypersonic Flow," AIAA Paper 89-1977, June 1989.

[29]van Leer, B., "Flux-Vector Splitting For the Euler Equations," Inst. for Computer Applications in Science and Engineering, ICASE TR 82-30, Hampton, VA, Sept. 1982.

[30]Anderson, W., Thomas, J., and van Leer, B., "A Comparison of Finite Volume Flux Vector Splittings for the Euler Equations," AIAA Paper 85-0122, Jan. 1985.

[31]Wright, M., Sinha, K., Olejniczak, J., Candler, G., Magruder, T., and Smits, A., "Numerical and Experimental Investigation of Double-Cone Shock Interactions," *AIAA Journal*, Vol. 38, No. 12, 2000, pp. 2268–2276.

[32]Edney, B., "Anomalous Heat Transfer and Pressure Distributions on Blunt Bodies at Hypersonic Speeds in the Presence of an Impinging Shock," Aeronautical Research Inst. of Sweden, TR 115, Stockholm, Feb. 1968.

[33]Delery, J., and Marvin, J., "Shock-Wave Boundary Layer Interactions," AGARD Rept. 280, April 1986.

[34]Harvey, J., Holden, M., and Wadhams, T., "Code Validation Study of Laminar Shock/Boundary Layer and Shock/Shock Interactions in Hypersonic Flow. Part B: Comparison with Navier–Stokes and DSMC Solutions," AIAA Paper 2001-1031, Jan. 2001.

[35]Gaitonde, D., Canupp, P., and Holden, M., "Evaluation of an Upwind-Biased Method in a Laminar Hypersonic Viscous/Inviscid Interaction," AIAA Paper 2001-2859, June 2001.

[36]Chapman, D., Kuehn, D., and Larson, H., "Investigation of Separated Flows in Supersonic and Subsonic Streams with Emphasis on the Effect of Transition," NACA TR 3869, March 1957.

[37]Adamson, T., and Messiter, A., "Analysis of Two-Dimensional Interactions Between Shock Waves and Boundary Layers," *Annual Review of Fluid Mechanics*, Vol. 12, 1980, pp. 103–138.

[38]Lewis, J., Kubota, T., and Lees, L., "Experimental Investigation of Supersonic Laminar, Two-Dimensional Boundary-Layer Separation in a Compresion Corner with and Without Cooling," *AIAA Journal*, Vol. 6, No. 1, 1968, pp. 7–14.